Amorphous and Nanocrystalline Soft Magnetic Materials — Michael McHenry, Chairman

Recent advances in the development of $(Fe,Co)_{88}M_7B_4Cu_1$ magnets (invited)

M. A. Willard,[a] D. E. Laughlin, and M. E. McHenry
Department of Materials Science and Engineering, Carnegie Mellon University, Pittsburgh, Pennsylvania 15213

Annealing of amorphous precursor alloys, with compositions $(Fe,Co)_{88}M_7B_4Cu_1$ (M=Zr, Nb, Hf), above their primary crystallization temperature results in the nanocrystallization of the ferromagnetic α'-FeCo phase. This work describes results of the characterization of these alloys, including morphological and chemical stability of the α'-FeCo phase, examination of alloy compositions, and development of a pseudo-Slater–Pauling curve for the amorphous precursor alloys. Samples with the composition $Fe_{44}Co_{44}Zr_7B_4Cu_1$ were annealed at 600 °C for 10, 31, 100, 308, 1000, and 3072 h in Ar and examined by x-ray diffraction (XRD) and transmission electron microscopy (TEM). Scherrer analysis of x-ray peak breadths was used to infer only a slight increase in the grain size of the sample annealed for 3072 h (~60 nm) compared to the samples annealed for short times (~40 nm). TEM studies revealed a distribution of grain sizes in the material with an average grain size of 42 nm for the 3072 h annealed sample. Samples annealed at higher temperatures exhibited the additional minority phases $(Fe,Co)_3Zr$ and ZrO. XRD analysis of the samples annealed for extended times at 600 °C do not indicate any formation of these phases, even in the sample annealed for 3072 h. TEM indicates the formation of minority phases, probably resulting from the devitrification of the amorphous grain-boundary phase and/or oxidation upon extended annealing. Differential scanning calorimetry results on alloys of composition $(Fe_{0.5}Co_{0.5})_{89}Zr_7B_4$ and $(Fe_{0.65}Co_{0.35})_{88}Zr_7B_4Cu_1$ show primary crystallization temperatures of 495 and 480 °C, respectively. © *2000 American Institute of Physics.* [S0021-8979(00)77508-6]

I. INTRODUCTION

Recently, premiere soft magnetic alloys have been developed with two-phase microstructures consisting of nanocrystalline ferromagnetic grains surrounded by a ferromagnetic amorphous phase. These alloys include $Fe_{73.5}Si_{13.5}B_9Nb_3Cu_1$ (FINEMET) by Yoshizawa, Ogurna, and Yamauchi,[1] and $Fe_{88}Zr_7B_4Cu_1$ (NANOPERM) by Suzuki *et al.*[2] The FINEMET and NANOPERM alloys rely on the α-Fe_3Si ($D0_3$ structure) and α-Fe (bcc structure) nanocrystalline phases, respectively, for the averaging of the magnetocrystalline anisotropy and magnetostrictive coefficients of the nanocrystalline phase over the many small grains of the material. During the past two years, our group at Carnegie Mellon University has developed a nanocrystalline soft magnetic material, called HITPERM. This alloy has nanocrystalline α'-FeCo ($B2$ structure) as the primary phase and is produced by nanocrystallization of amorphous precursors of composition $(Fe,Co)_{88}M_7B_4Cu_1$ (M=Zr, Nb, Hf).

The HITPERM alloy has been examined for its potential as a material for high-temperature soft-magnetic applications.[3,4] For these types of applications, it is imperative that additional phases do not form and that grain growth is minimal. This is due in part to the need for small grains to take advantage of averaging of random magnetic anisotropy over many grains so that excellent extrinsic soft magnetic properties are maintained. The Herzer model[5] considers the influence of averaging of the random magnetic anisotropy over a volume equal to the cube of the magnetic exchange length L_{ex}. In the Herzer model, the technical magnetic property of interest, the coercivity H_c is predicted to scale as

$$H_c \sim K_1^4 D^6 / A^3, \tag{1}$$

where K_1 denotes the first term in the angular expansion of magnetocrystalline anisotropy energy density, A the exchange stiffness, and D the grain size. For the case of these FeCo-based alloys, where the parameters $K_1 = 8\ \mathrm{kJ/m^3}$ and $A \sim 1.7 \times 10^{-11}\ \mathrm{J/m}$, a coercivity of 79.6 A/m (1 Oe) corresponds to a maximum average grain size of 21 nm.[4] At higher temperatures, these requirements should be less restrictive due to the lowering of the magnetocrystalline anisotropy with temperature.

Deleterious increases in the coercivity may be caused by grain growth, second-phase formation that can inhibit domain-wall motion, and residual stress that leads to magnetostrictive effective anisotropies. Soft-magnetic properties will degrade if morphological or phase instabilities at el-

[a]Electronic mail: mw4t@andrew.cmu.edu

evated temperatures result in nanocrystal coarsening and/or devitrification or crystallization of the intergranular amorphous phase of these alloys. X-ray diffraction (XRD) and transmission electron microscopy (TEM) have been employed as structural and microstructural probes on samples annealed at different temperatures and for different times.

In this article, we report on studies of the phase stability in HITPERM materials, as well as preliminary results for alloy compositions and development of a pseudo-Slater–Pauling curve for the amorphous precursors of these nanocrystalline alloys.

II. EXPERIMENTAL PROCEDURE

Amorphous alloy precursors were prepared by a single-roller melt-spinning technique, using high-purity arc-melted ingots as the starting material.[3] The as-cast ribbons of composition $(Fe_{0.5}Co_{0.5})_{88}Zr_7B_4Cu_1$ were then annealed at 600 °C for 10, 31, 100, 308, 1000, and 3072 h in quartz ampoules with an argon atmosphere. The crystal structure and grain sizes of the annealed ribbons were examined by XRD using a Rigaku Θ/Θ diffractometer employing Cu $K\alpha$ radiation. Grain sizes were estimated from XRD peak breadths using a standard Scherrer analysis.[6] TEM was used on selected ribbons for grain-size measurement and minority-phase identification. These experiments were performed using a JEOL 120 CX TEMSCAN microscope. Differential scanning calorimetry was performed on amorphous ribbons with compositions $(Fe_{0.5}Co_{0.5})_{89}Zr_7B_4$ and $(Fe_{0.65}Co_{0.35})_{88}Zr_7B_4Cu_1$ to determine the primary crystallization temperatures using a Perkin Elmer DSC7. The scans ranged from 50 to 580 °C with a heating rate of 0.167 °C/s. For thermomagnetic analysis, a Quantum Design superconducting quantum interference device (SQUID) magnetometer was used to measure the magnetization of samples in a saturating applied field of 1000 Oe and over a temperature range of 4–370 K.

III. RESULTS AND DISCUSSION

A. Grain size and chemical stability after long-term annealing

The x-ray diffraction peaks are broadened due to the small grain size. The semiempirical Scherrer analysis can be used to estimate the grain size for the diffraction peaks using the equation[6,7]

$$t = 0.9\lambda / B \cos \Theta_B , \tag{2}$$

where the grain thickness t is inversely proportional to the x-ray peak breadth B (in radians) and the cosine of the Bragg angle, Θ_B. As seen in Fig. 1, the XRD patterns of $(Fe_{0.5}Co_{0.5})_{88}Zr_7B_4Cu_1$ samples annealed at 600 °C for various times shows relatively broad peaks. The Scherrer analysis for long annealing times reveals an average grain size of ~60 nm. The Scherrer analysis for these alloys is summarized in Table I. Further, Fig. 1 yields only the diffraction peaks corresponding to the fundamental scattering peaks of the α'-FeCo phase.

Figure 2(a) shows a bright-field TEM image of the HITPERM $(Fe_{0.5}Co_{0.5})_{88}Zr_7B_4Cu_1$ ribbon annealed for 3072 h.

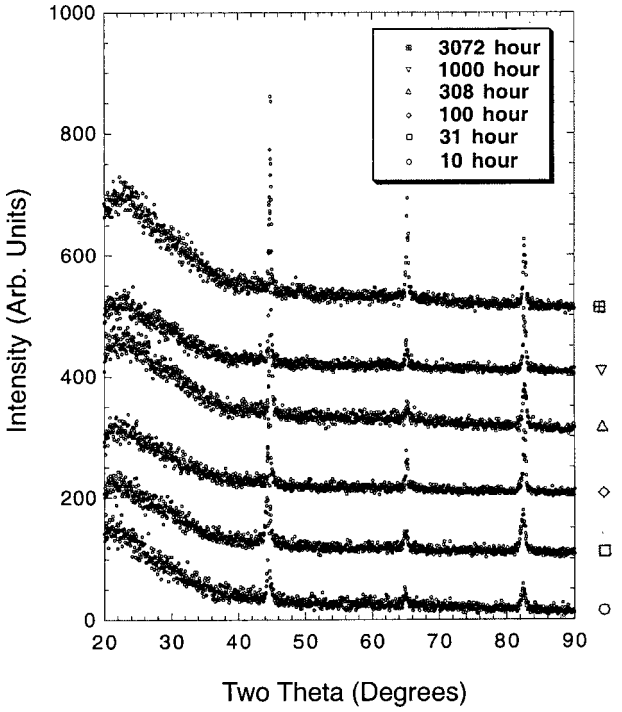

FIG. 1. X-ray diffraction pattern for HITPERM samples annealed at 600 °C for 10, 31, 100, 308, 1000, and 3072 h, showing the broadened fundamental x-ray diffraction peaks for α'-FeCo.

Figure 2(a) shows some contrast, but it is not easy to distinguish individual grains from one another. Bright-field/dark-field pairs were used to determine the grain sizes of the α'-FeCo phase. A typical dark-field image [corresponding to the bright-field image of Fig. 2(a)] is illustrated in Fig. 2(b). A range of grain sizes can be inferred from this image, including a single grain that is uncharacteristically large (or possibly two smaller grains with similar orientations). The dark-field image was taken placing a small aperture over a portion of the α'-FeCo (110) diffraction ring and recording the corresponding image. The grain size distribution measured for this sample is indicated in Fig. 3 with an average grain size of 42 nm for the ribbon annealed for 3072 h. The discrepancy between the Scherrer analysis and TEM observations is due in part to the sample preparation method for TEM and grain-size distribution of the ribbon (surface grains being larger on the side of the ribbon farthest from the quench wheel). The XRD experiment yields broadening from the grains on the surface of the ribbon and in the bulk. This analysis is, therefore, an average grain size of the two

TABLE I. Grain size, as determined by Scherrer analysis of broadened x-ray diffraction peaks for samples with composition $(Fe_{0.5}Co_{0.5})_{88}Zr_7B_4Cu_1$.

Annealing time (h)	D_{mean} (nm)	σ (nm)
10	49	17
31	37	10
100	71	13
308	58	33
1000	57	9
3072	61	14

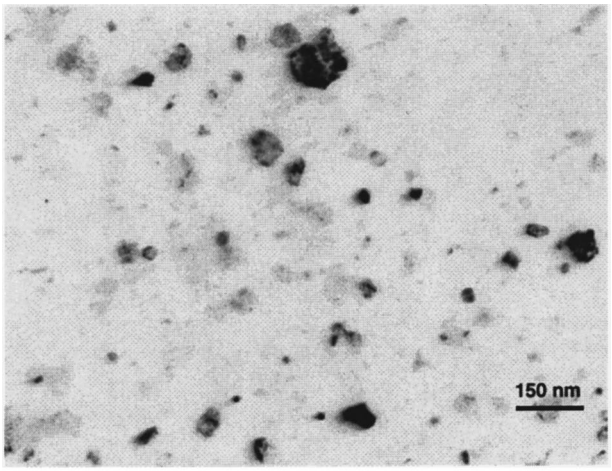

(a)

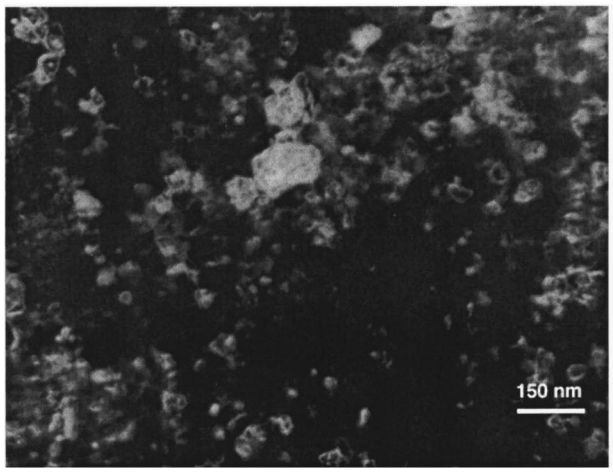

(b)

FIG. 2. (a) Dark-field negative image of the HITPERM sample annealed at 600 °C for 3072 h. (b) Bright-field negative image.

regions. The TEM sample preparation allows a probe of the side of the ribbon closest to the wheel, hence, the smaller grain size.

The electron diffraction pattern of Fig. 4 shows additional phases that were not observable in the XRD experiments. Electron diffraction can be more sensitive than the

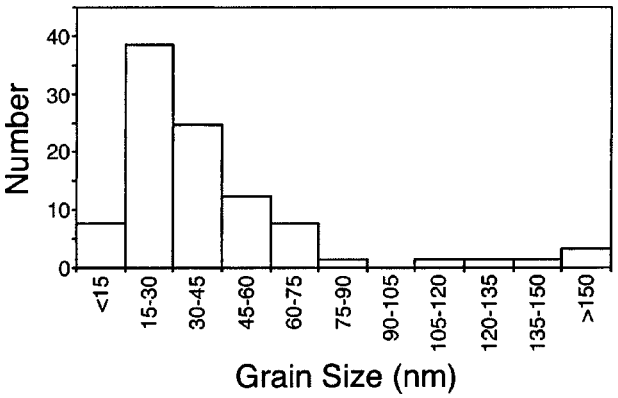

FIG. 3. Grain-size distribution as determined by bright-field/dark-field pairs for the HITPERM sample annealed at 600 °C for 3072 h.

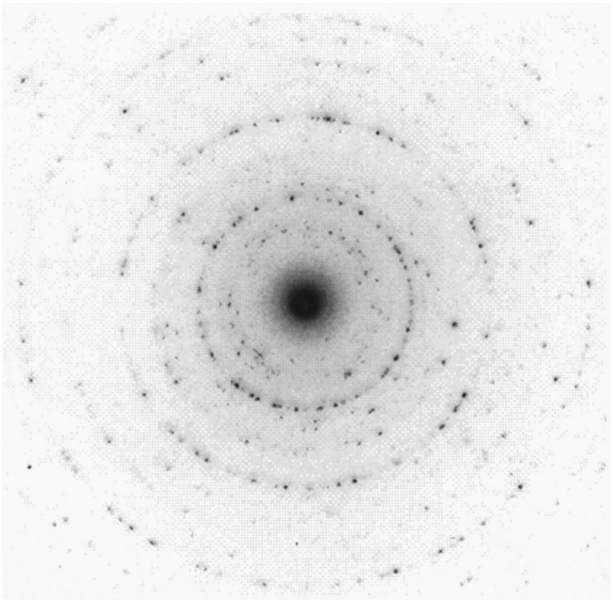

FIG. 4. Diffraction pattern for the sample shown in Fig. 2. The dark-field image was taken using a portion of the first strong diffraction ring (camera constant of 760 mm).

x-ray diffraction in identifying minority secondary phases because of the smaller volume examined. The peak intensity was mapped from the diffraction patterns using a routine written in the IDL programming language. This routine calculates the circumferentially integrated diffracted intensity as a function of position in the radial direction (in reciprocal space), as averaged over the full diffraction circle, for a given radius (wave vector). Such a radial intensity function is illustrated in Fig. 5. Simulations of some possible phases, including Fe_2O_3, ZrO, and $(Fe,Co)_3Zr$, corresponding to the diffraction peaks in Fig. 5 are found in Figs. 6(a)–6(c). Although no magnetic analysis has yet been performed for these particular samples, it is expected that second-phase oxides will be detrimental to the soft-magnetic properties. The inhibited grain growth in these alloys may be a product of

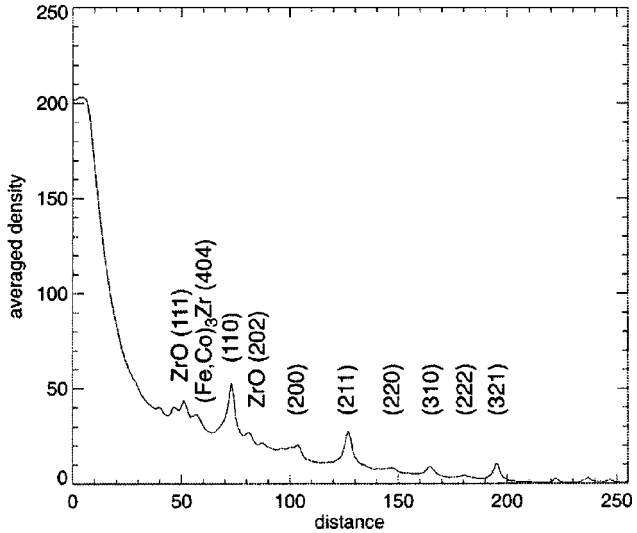

FIG. 5. Radial function of the electron diffraction peak intensity from the diffraction pattern in Fig. 4.

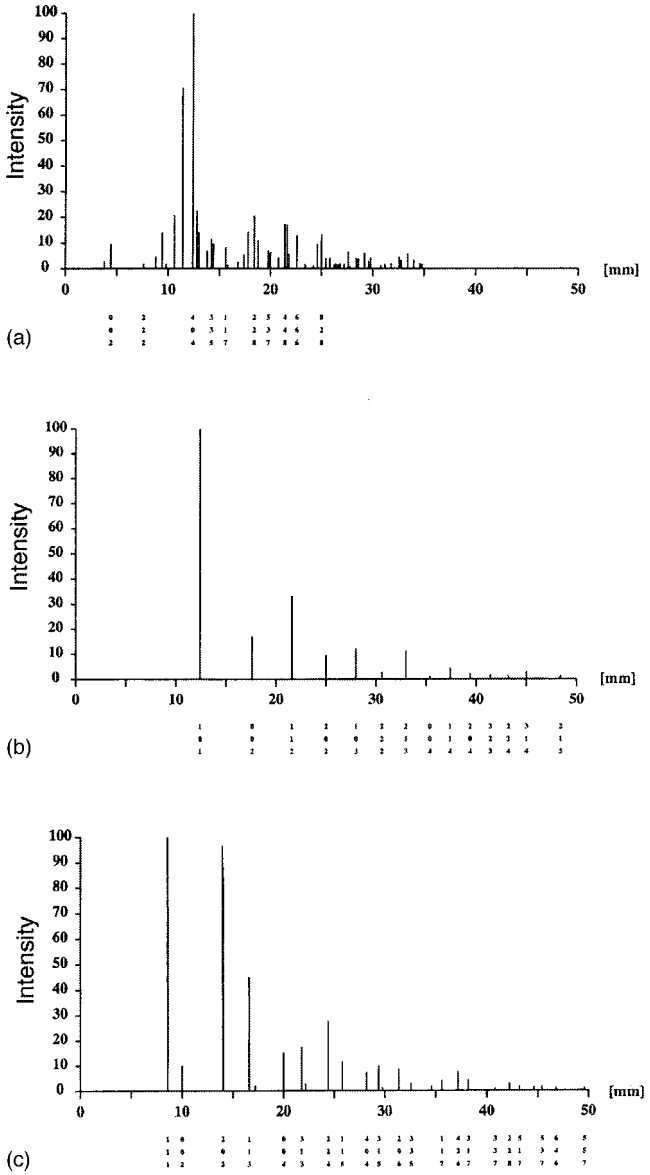

FIG. 6. (a)–(c) Simulations using EMS software of the possible phases present by examination of the electron diffraction pattern for the sample annealed for 3072 h. (a) $(Fe,Co)_3Zr$. (b) α'-FeCo. (c) ZrO.

the preferential oxidation of the Zr-rich amorphous grain-boundary phase. More experiments will have to be performed to determine the exact morphology of the secondary phases and whether they are situated at (and pin) the grain boundaries. Figure 7 shows XRD data that indicates the formation of a ZrO phase for ribbons annealed at the much higher 945 °C for 1 h. These data support the TEM diffraction data for the sample annealed for 3072 h at the lower 600 °C temperature.

In previous investigations, synchrotron x-ray diffraction showed the ordered α'-FeCo as the primary nanocrystalline phase for a $(Fe_{0.5}Co_{0.5})_{88}Zr_7B_4Cu_1$ sample annealed at 650 °C for 1 h.[2] This is not surprising considering the equilibrium binary Fe–Co phase diagram, where the order/disorder phase transformation occurs at 730 °C. Figure 8 shows a synchrotron x-ray diffraction pattern for a $(Fe_{0.5}Co_{0.5})_{88}Zr_7B_4Cu_1$ sample annealed at 550 °C for 1 h.

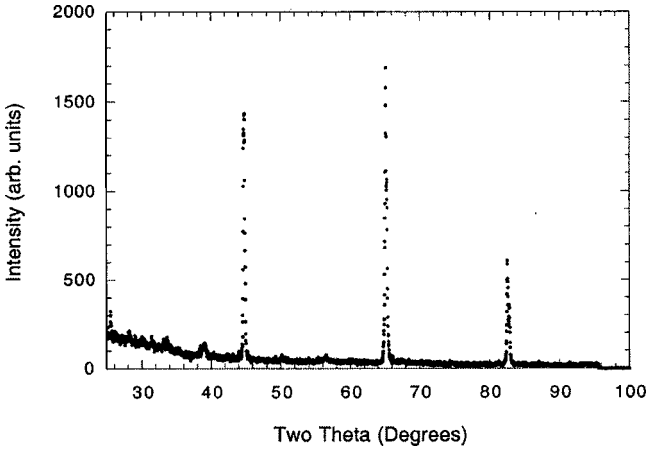

FIG. 7. X-ray diffraction pattern of a $(Fe_{0.5}Co_{0.5})_{88}Zr_7B_4Cu_1$ sample annealed at 945 °C for 1 h, showing ZrO diffraction peaks (in addition to the α'-FeCo peaks).

This sample shows the (100) superlattice reflection, corresponding to the ordered α'-FeCo phase. This result supports the contention that the sample annealed at 600 °C for 3072 h as being the α'-FeCo phase. We might also expect to see superlattice peaks in the electron diffraction pattern. However, the superlattice peaks are predicted to be four orders of magnitude smaller by kinematic simulations and one order of magnitude smaller by dynamical simulations than the fundamental reflections, therefore, the superlattice reflections are extremely difficult to observe in TEM. The simulation for the kinematic theory is shown in Fig. 6(b), where the superlattice reflections are not observed because of low intensities (and, therefore, not labeled).

B. Differential scanning calorimetry of HITPERM alloys

Our first step in the characterization of nanocrystalline alloys with these compositions is the determination of their crystallization temperature. HITPERM amorphous precursors with compositions excluding Cu and other alloy compositions with different Fe:Co ratios, were meltspun at the Naval Research Laboratory. The alloy compositions were

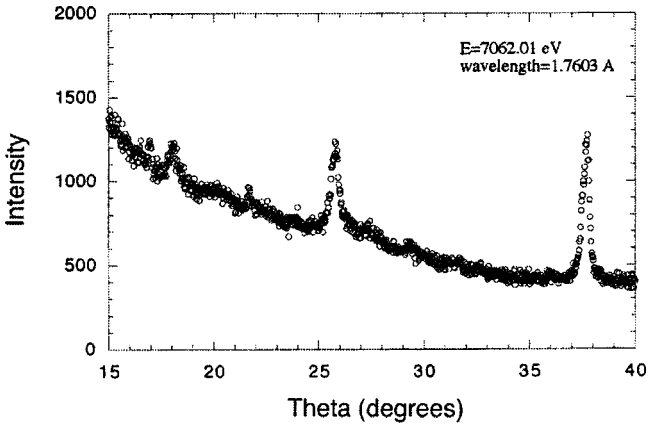

FIG. 8. Synchrotron x-ray diffraction of a sample annealed at 550 °C for 1 h. This diffraction pattern shows the α'-FeCo (100) superlattice reflection.

TABLE II. Crystallization temperatures for various nanocrystalline soft magnetic materials.

Sample	T_{x1} (°C)	T_{x2} (°C)	References
$(Fe_{0.5}Co_{0.5})_{89}Zr_7B_4$	495	...	...
$(Fe_{0.65}Co_{0.35})_{88}Zr_7B_4Cu_1$	480	...	...
$(Fe_{0.5}Co_{0.5})_{88}Zr_7B_4Cu_1$	510	700	3
$Fe_{86}Zr_7B_6Cu_1$	527	722	8 and 9
$Fe_{89}Zr_7B_4$	519–536	707–710	10, 11, and 12
$Fe_{73.5}Si_{13.5}Nb_3B_9Cu_1$	497–539	633–689	13, 14, and 15

$(Fe_{0.5}Co_{0.5})_{89}Zr_7B_4$ and $(Fe_{0.65}Co_{0.35})_{88}Zr_7B_4Cu_1$. The primary crystallization temperatures for these alloys as determined by differential scanning calorimetry, are summarized in Table II,[3,8–15] along with data from other studies on Fe-based and FeCo-based nanocrystalline alloys. A useful tool in discussing these compositions may be to compare them to the most heavily studied HITPERM composition $(Fe_{0.5}Co_{0.5})_{88}Zr_7B_4Cu_1$. The increase of the Fe:Co ratio from 1:1 to 13:7 in these alloys results in lower primary crystallization temperature. Also, removing 1 at. % Cu and increasing the ferromagnetic transition-metal species (Fe,Co) in $(Fe_{0.5}Co_{0.5})_{89}Zr_7B_4$ yields a decrease in the crystallization temperature.

C. Magnetization of the amorphous precursors to HITPERM and NANOPERM alloys

As seen in Fig. 9, thermomagnetic data have been collected for four amorphous alloys of compositions $(Fe_{1-x}Co_x)_{88}Zr_7B_4Cu_1$ ($x=0$, 0.35, 0.5, and 0.91). These alloys are the precursors to the NANOPERM and HITPERM nanocrystalline alloys. The specific magnetization, extrapolated to 0 K, shows a systematic variation with composition. The temperature dependence of the magnetization is also strongly temperature dependent for the Fe-based NANOPERM precursor with a Curie temperature of ~300 K. However, the FeCo-based HITPERM precursors maintain a largely temperature-invariant magnetic moment for $T<400$ K. This is reflective of their much higher Curie temperatures. In fact, previous work has shown that for the

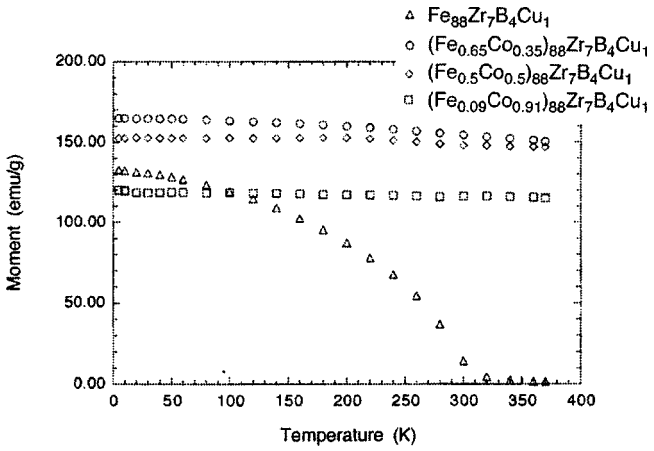

FIG. 9. (a) and (b) specific magnetization as a function of temperature for the amorphous alloys $(Fe_{1-x}Co_x)_{88}Zr_7B_4Cu_1$ ($x=0$, 0.35, 0.5, and 0.91).

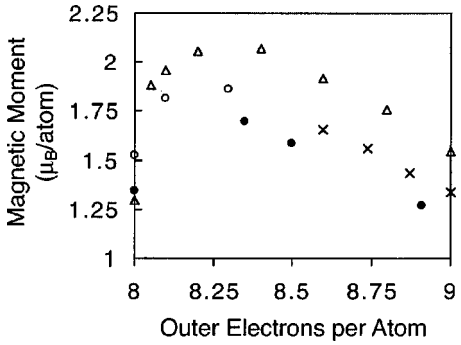

FIG. 10. Pseudo-Slater–Pauling curve for $(Fe,Co)_{88}Zr_7B_4Cu_1$ amorphous precursor alloys (●). Other data correspond to values taken from: Ohnuma *et al.* (Ref. 16) (△) for $(Fe,Co)_{90}Zr_{10}$; O'Handley, Mandelsohn, and Nesbitt (Ref. 17) (×) for $(Fe,Co)_{80}B_{20}$; and Iwanabe *et al.* (Ref. 4) (○) for $(Fe,Co)_{88}Hf_7B_4Cu_1$.

$(Fe_{0.5}Co_{0.5})_{88}Zr_7B_4Cu_1$ precursor, the Curie temperature of the amorphous phase can be inferred to be much larger than the crystallization temperature of the α'-FeCo phase.[3]

An interesting manifestation of the low-temperature magnetization data is seen by plotting the magnetic dipole moment per atom (in Bohr magnetons) as a function of alloy composition in terms of the average magnetic transition-metal valence. This leads to a pseudo-Slater–Pauling curve for the amorphous alloys. As seen in Fig. 10,[3,16,17] the data show a striking resemblance to that of the Slater–Pauling curve for bulk crystalline alloys. A peak in the magnetic moment per atom occurs at a composition near $Fe_{65}Co_{35}$ in good agreement with the behavior seen for binary FeCo crystalline alloys. Other amorphous alloy compositions are also shown to reveal that this peak does, in fact, shift to lower moments for other FeCo-based metallic glasses, presumably due to the large concentrations of glass-forming elements in the same.

IV. CONCLUSIONS

Scherrer analysis of x-ray peak breadth was used to infer only a slight increase in the grain size of a sample with composition $Fe_{44}Co_{44}Zr_7B_4Cu_1$ annealed for 3072 h at 600 °C. The grain size as determined by XRD for a sample annealed for 3072 h was ~60 nm compared to the samples annealed for short times with grain sizes of ~40 nm. TEM studies revealed a distribution of grain sizes in the material with an average grain size of 42 nm for the sample annealed for 3072 h. Samples annealed at higher temperatures exhibited additional minority phases $(Fe,Co)_3Zr$ and ZrO. XRD analysis of the samples annealed for extended times at 600 °C do not indicate any formation of these phases, even in the sample annealed for 3072 h. TEM does indicate the formation of minority phases, probably resulting from the devitrification of the amorphous grain-boundary phase and/or oxidation upon extended annealing. Differential scanning calorimetry results on alloys of composition $(Fe_{0.5}Co_{0.5})_{89}Zr_7B_4$ and $(Fe_{0.65}Co_{0.35})_{88}Zr_7B_4Cu_1$, show primary crystallization temperatures of 495 and 480 °C, respectively.

ACKNOWLEDGMENTS

Effort sponsored by the Air Force Office of Scientific Research, Air Force Materiel Command, USAF, under Grant No. F49620-96-1-0454. The U.S. Government is authorized to reproduce and distribute reprints for Governmental purposes notwithstanding any copyright notation thereon. One of the authors (D.E.L.) acknowledges partial support from a NEDO grant. The authors would like to thank Vince Harris and Badri Das (Naval Research Laboratory) for their assistance in alloy synthesis and Marc DeGraef for his assistance with IDL and TEM analysis.

[1] Y. Yoshizawa, S. Oguma, and K. Yamauchi, J. Appl. Phys. **64**, 6044 (1988).
[2] K. Suzuki, A. Makino, N. Kataoka, A. Inoue, and T. Masumoto, Mater. Trans., JIM **32**, 93 (1991).
[3] M. A. Willard, D. E. Laughlin, M. E. McHenry, D. Thoma, K. Sickafus, J. O. Cross, and V. G. Harris, J. Appl. Phys. **84**, 6773 (1998).
[4] H. Iwanabe, B. Lu, M. E. McHenry, and D. E. Laughlin, J. Appl. Phys. **85**, 4424 (1999).
[5] G. Herzer, IEEE Trans. Magn. **26**, 1397 (1990).
[6] P. Scherrer, Nachrichten Gesellschafts Wissenschaftlich Göttingen **2**, 96 (1918).
[7] F. W. Jones, Proc. R. Soc. London, Ser. A **166**, 16 (1938).
[8] N. Shiga, F. Kogiku, and M. Yukumoto, Mater. Trans., JIM **36**, 939 (1995).
[9] K. Suzuki, M. Kikuchi, A. Makino, A. Inoue, and T. Masumoto, Mater. Trans., JIM **32**, 961 (1991).
[10] Y. K. Kim, T. H. Noh, I. K. Kang, and T. Kang. Mater. Sci. Eng., A **179/180**, 552 (1994).
[11] K. Suzuki, N. Kataoka, A. Inoue, A. Makino, and T. Masumoto, Mater. Trans., JIM **31**, 743 (1990).
[12] M. Kopcewicz, A. Grabias, and D. L. Williamson, J. Appl. Phys. **82**, 1747 (1997).
[13] S. H. Kim, W. K. Pi, T. H. Noh, H. J. Kim, and T. K. Kang, J. Appl. Phys. **73**, 6591 (1993).
[14] T. H. Noh, M. B. Lee, H. J. Kim, and I. K. Kang, J. Appl. Phys. **67**, 5568 (1990).
[15] N. Kataoka, A. Inoue, T. Masumoto, Y. Yoshizawa, and K. Yamauchi, Jpn. J. Appl. Phys., Part 2 **28**, L1820 (1989).
[16] S. Ohnuma, K. Shirakawa, M. Nose, and T. Masumoto, IEEE Trans. Magn. **MAG-16**, 1129 (1980).
[17] R. C. O'Handley, L. I. Mendelsohn, and E. A. Nesbitt, IEEE Trans. Magn. **MAG-12**, 942 (1976).